Wavenumber-Domain Autofocusing for Highly Squinted UAV SAR Imagery

Lei Zhang, Jialian Sheng, Mengdao Xing, *Member, IEEE*, Zhijun Qiao, *Member, IEEE*, Tao Xiong, and Zheng Bao, *Senior Member, IEEE*

***Abstract*—Being capable of enhancing the flexibility and observing ability of synthetic aperture radar (SAR), squint mode is one of the most essential operating modes in SAR applications. However, processing of highly squinted SAR data is usually a challenging task attributed to the spatial-variant range cell migration over a long aperture. The *Omega-k* algorithm is generally accepted as an ideal solution to this problem. In this paper, we focus on using the wavenumber-domain approach for highly squinted unmanned aerial vehicle (UAV) SAR imagery. A squinted phase gradient autofocus (SPGA) algorithm is proposed to overcome the severe motion errors, including phase and nonsystematic errors. Herein, the inconsistence of phase error and range error in the squinted wavenumber-domain imaging is first presented, which reveals that even the motion error introduces very small phase error, it causes considerable range error due to the Stolt mapping. Based on this, two schemes of SPGA-based motion compensation are developed according to the severity of motion error. By adapting the advantages of weighted phase gradient autofocus and quality phase gradient autofocus, the robustness of SPGA is ensured. Real measured data sets are used to validate the proposed approach for highly squinted UAV-SAR imagery.**

***Index Terms*—High squinted SAR, motion compensation (MoCo), squinted phase gradient autofocus (SPGA), synthetic aperture radar (SAR), unmanned aerial vehicle (UAV).**

I. Introduction

UNMANNED aerial vehicle (UAV) synthetic aperture radar (SAR) is a preferable remote sensing system for achieving high-resolution microwave images of the interesting scene. And by pointing at an angle from broadside, squint mode is potential to increase the flexibility of UAV-SAR. In squinted UAV-SAR applications, the interesting wide area could be observed within a single pass of the UAV, which dramatically relaxes the trajectory design. However, in squinted UAV-SAR processing, two significant factors should be accounted carefully. The first factor in highly squinted UAV-SAR processing is the correction of range cell migration (RCM). In squint mode, the spatial-variant RCM becomes much more serious than broadside mode. Conventional squinted image formations are generally limited by approximations, such as range-Doppler algorithm (RDA) and polar format algorithm (PFA) [1], resulting in serious image degradations as blurring and resolution loss. The problem stems from higher order range-azimuth coupling effect in the phase of the squinted SAR transfer function. This coupling effect is usually resolved or reduced by introducing the processing of secondary range compression (SRC) in chirp scaling algorithm (CSA) and its extensions [1]–[4]. However, involving some approximations, CSAs are also limited by squint angle and wavelength. The *Omega-k* algorithm [5], [6] is commonly accepted as an ideal approach to the highly squinted SAR imagery, because *Omega-k* algorithm involves no approximation in RCM correction. And in terms of efficiency and flexibility improvement, some modifications of *Omega-k* algorithm have been proposed [5]–[10]. However, a well-known shortcoming of *Omega-k* algorithm is its inconsistence with motion compensation (MoCo) procedure [8], [9], which may limit its applications in UAV-SAR imagery. The second factor in highly squinted UAV-SAR processing lies in the presence of strong motion error. Due to small size and weight, UAV is very sensitive to atmospheric turbulence, resulting in serious trajectory deviations, and angular deviations, including roll, pitch, yaw angles errors. The angular deviations induce not only the antenna illumination roll-off effects [11] but also possible focusing degradation. In real situations, the angular deviations are corrected by using antenna stabilization [12] and Doppler centroid correction [13]–[15]. The trajectory deviations are usually corrected by precise motion compensation (MoCo) by using measurements from a high-accuracy inertial navigation system/inertial measurement unit (INS/IMU). However, these measurements would be unavailable, since miniaturization of UAV-SAR system is a very essential objective. As a result, for the UAV-SAR imagery, MoCo strategies based on autofocus approaches are advisable. And some novel autofocus schemes have been proposed based on broadside SAR geometry [16], [17].

In this paper, we propose an autofocus approach marrying with a squinted *Omega-k* algorithm for highly squinted UAV-SAR imagery. By adapting the idea of extend *Omega-k* (EOK) algorithm [8], [9], a modified Stolt mapping (SM) is applied in the squinted *Omega-k* algorithm, which removes the coupling terms between range and azimuth wavenumbers, namely, the RCM, but preserves the azimuth phase terms. Then, autofocus processing is combined into the in the *Omega-k* image formation. The effect of the modified SM on the motion

Manuscript received October 04, 2011; accepted October 25, 2011. Date of publication November 08, 2011; date of current version April 18, 2012. This work was supported by "973" Program of China under Grant 2010CB731903. The associate editor coordinating the review of this paper and approving it for publication was Prof. Ralph Etienne-Cummings.

L. Zhang, J. Shen, M. Xing, T. Xong, and Z. Bao are with the National Key Lab of Radar Signal Processing, Xidian University, Xi'an 710071, China (e-mail: zhanglei_0330@126.com; S.jialian@gmail.com; Xmd@xidian.edu.cn; zhbao@xidian.edu.cn).

Z. Qiao is with the Department of Mathematics, University of Texas–Pan American, Edinburg, TX 78539-2999 USA (e-mail: qiao@utpa.edu).

Color versions of one or more of the figures in this paper are available online at http://ieeexplore.ieee.org.

Digital Object Identifier 10.1109/JSEN.2011.2175216

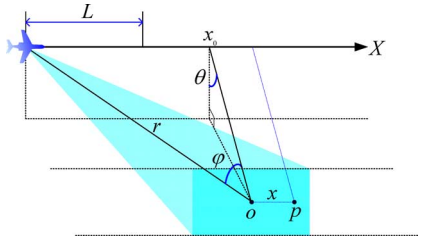

Fig. 1. Geometry of squinted SAR.

error is analyzed in detail by using the principle of stationary phase (POSP) and we can note that the modified SM would amplified the range error dramatically, while it preserves the phase error. Based on this, a squinted phase gradient autofocus (SPGA) algorithm is developed to estimate the motion error for highly squinted UAV-SAR. In SPGA, azimuth deramping is applied firstly to convert the signal into spotlight representation. And the azimuth-dependent quadratic phase due to high squint angle is accounted in the phase gradient estimate for each target sample. By SPGA, the motion error can be retrieved from the phase error and the amplified range error can be also retrieved. Then, MoCo is performed in an iterative manner. The MoCo strategy is not only able to cope with squinted UAV-SAR data in spotlight mode, but also stripmap mode with some modifications.

The paper is organized as follows: Section II gives the signal and geometry model of the highly squinted UAV-SAR and the squinted *Omega-k* algorithm is introduced. Section III presents a clear description of the SPGA and its detailed implementation in both highly squinted spotlight and stripmap modes. In Section IV, we present the experimental results with real data sets and some conclusions in the last section.

II. Wavenumuber-Domain Squint SAR Imaging Algorithms

A. Squinted Point Target Reference Spectrum

In this section, we focus on establishment of a wavenumber-domain imaging approach for highly squinted SAR. The squinted SAR geometry is shown in Fig. 1 referring to the conical processing geometry [17]. Considering ideal case without motion error (the motion error case will be discussed in the following content), a SAR sensor travels along a straight-line flight path during a synthetic aperture length L. And the velocity of platform is constant. The ideal linear trajectory is defined as X-axis corresponding to the azimuth direction. During the data acquisition, the radar beam directs at an offset angle (squint angle) φ. Symbol o denotes the scene center and the range from o to radar at φ is r. Symbol P denotes a target at the line through scene center and parallel with the trajectory. The distance between P and o is given by x. The instantaneous range from P to radar in the conical coordinate system is

$$R(X)=\sqrt{(r\cos\varphi)^2+(X-x-x_0)^2}$$
$$\text{and}\quad x_0=r\sin\varphi,\quad -\frac{L}{2}\le X\le\frac{L}{2}. \tag{1}$$

During the data acquisition, the transmitted pulsed chirp signal is

$$s_t(\tau)=\text{rect}\left(\frac{\tau}{T_p}\right)\cdot\exp\left[j2\pi\left(f_c\tau+\frac{\alpha\tau^2}{2}\right)\right] \tag{2}$$

where α is the chirp rate, T_p is the pulse duration width; τ denotes range fast-time. After downconversion to the base-band, the received signal from P is given by

$$s(\tau,X)=\varepsilon_p\cdot\text{rect}\left(\frac{\tau-\Delta t}{T_p}\right)\cdot\text{rect}\left(\frac{X-x_0-x}{L}\right)\times\exp\left[j2\pi\left(-f_c\Delta t+\frac{\alpha(\tau-\Delta t)^2}{2}\right)\right] \tag{3}$$

where $\Delta t = 2R(X)/c$ corresponds to the round-way time delay from radar to P and ε_p corresponds to the complex-valued scattering amplitude of the target. Applying Fourier transform (FT) with respect to τ, the signal is transferred into the range wavenumber domain. Omitting the constants introduced, it yields

$$\begin{aligned}&S(K_r,X)\\&=\int s(\tau,X)\ \exp(-j\Delta K_r\tau)d\tau\\&=\varepsilon_p\cdot\text{rect}\left(\frac{\Delta K_r}{4\pi\alpha T_p}\right)\cdot\text{rect}\left(\frac{X-x_0-x}{L}\right)\\&\quad\times\exp\left[j\frac{(K_r-K_{rc})^2c^2}{16\pi\alpha}\right]\\&\quad\times\exp\left[-jK_r\cdot\sqrt{(r\cos\varphi)^2+(X-x-r\sin\varphi)^2}\right]\end{aligned} \tag{4}$$

where K_r represents the range wavenumber $K_r = K_{rc}+\Delta K_r$, range wavenumber center $K_{rc}=4\pi f_c/c$, $\Delta K_r \in [-2\pi\alpha T_p/c, 2\pi\alpha T_p/c]$. The first exponential term in (4) corresponds to the waveform, and range matched filtering can be obtained by multiplying $s_r(K_r,X)$ by $\exp\left[-j(K_r-K_{rc})^2c^2/16\pi\alpha\right]$, and we have

$$\begin{aligned}&S_{MF}(K_r,X)\\&=\varepsilon_p\cdot\text{rect}\left(\frac{\Delta K_r}{4\pi\alpha T_p}\right)\cdot\text{rect}\left(\frac{X-x_0-x}{L}\right)\\&\quad\times\exp\left[-jK_r\cdot\sqrt{(r\cos\varphi)^2+(X-x-r\sin\varphi)^2}\right].\end{aligned} \tag{5}$$

To obtain the two-dimensional (2D) point target reference spectrum (PTRS), we apply FT in azimuth to (5), i.e.,

$$\begin{aligned}&S_{MF}(K_r,K_x)\\&=\int S_{MF}(K_r,X)\ \exp(-jK_xX)dX\\&=\int\varepsilon_p\cdot\text{rect}\left(\frac{\Delta K_r}{4\pi\alpha T_p}\right)\cdot\text{rect}\left(\frac{X-x_0-x}{L}\right)\\&\quad\times\exp\left[-jK_r\cdot\sqrt{(r\cos\varphi)^2+(X-x-r\sin\varphi)^2}\right]\\&\quad\times\exp(-jK_xX)\,dX.\end{aligned} \tag{6}$$

To deduce the analytic expression of PTRS, POSP [19] is ready to be used. Equating the first derivative of the phase function with respect to X in (6) to zero gives

$$K_r \frac{(X - x - r\sin\varphi)}{\sqrt{(r\cos\varphi)^2 + (X - x - r\sin\varphi)^2}} + K_x = 0. \quad (7)$$

Solving the above equation, the stationary point yields

$$X^* = -\frac{K_x}{\sqrt{K_r^2 - K_x^2}} r\cos\varphi + x + r\sin\varphi. \quad (8)$$

Then, we substitute X^* for X in the phase function of (6). Omitting the constants, the PTRS is given by

$$\begin{aligned} S_{MF}(K_r, K_x) &= \varepsilon_p \cdot \mathrm{rect}\left[\frac{(K_r - K_{rc})}{4\pi\alpha T_p}\right] \cdot \mathrm{rect}\left(\frac{K_x - K_{xc}}{\Delta K_x}\right) \\ &\quad \times \exp\left\{-j\left[\left(\sqrt{K_r^2 - K_x^2}\cos\varphi + K_x\sin\varphi\right)\cdot r + K_x \cdot x\right]\right\} \end{aligned} \quad (9)$$

where ΔK_x denotes the azimuth wavenumber width and K_{xc} is the azimuth wavenumber center (corresponds to the Doppler center). It should be emphasized that the same PTRS expression can be also deduced by the equivalent wavelength concept [19]. From the exponential term in (9), the relevant portion of the 2D wavenumber domain phase is

$$\phi_{sq}(K_r, K_x) = -\sqrt{K_r^2 - K_x^2}\cos\varphi \cdot r - K_x \sin\varphi \cdot r - K_x \cdot x. \quad (10)$$

It consists of three terms. The last term in (10) is the linear phase corresponding to the azimuth position of the target. And the second term is the linear phase caused by squinted data acquisition introducing a relative offset in azimuth. While in the first term, the range and azimuth wavenumbers are coupled yielding the RCM. The first term is a function of the target's slant range representing the spatial variance of RCM. The PTRS in (10) corresponds to the pulsed chirp waveforms. However, when we consider frequency modulated continuous waveforms (FMCW), the two-dimension wavenumber expression should be different. For details about the PTRS of FMCW SAR, some novel works [20]–[22] can be consulted.

B. Omega-k and Extended Omega-k Algorithms

Clearly, the PTRS of non-squinted SAR is a special case of (9). With substituting $\varphi = 0$ into (10), we have the phase expression of non-squinted SAR.

$$\phi_{nsq}(K_r, K_x) = -\sqrt{K_r^2 - K_x^2} \cdot r - K_x \cdot x. \quad (11)$$

In the original *Omega-k* processing in [5], a change of variables is applied that

$$\sqrt{K_r^2 - K_x^2} \to K_{rc} + \Delta K_y. \quad (12)$$

It is called Stolt mapping, and usually implemented by interpolation. SM removes the range and azimuth wavenumber coupling in the phase, and thus RCM is corrected ideally. Moreover, high order phase terms corresponding to the azimuth wavenumber are also eliminated precisely. After SM, 2D inverse Fourier transform (IFT) is followed to focus the 2D SAR image. Although the *Omega-k* algorithm is accepted as ideal and high-accuracy approach for focusing SAR data, it is sensitive to motion error. Therefore, *Omega-k* algorithm is usually not applied to airborne SAR imagery, where serious trajectory deviations exist. To overcome the shortness of the standard *Omega-k* algorithm in airborne SAR applications, the novel extended *Omega-k* has been proposed in [8], [9]. Considering the broadside case, the modified SM in EOK is given by

$$\sqrt{K_r^2 - K_x^2} \to \sqrt{K_{rc}^2 - K_x^2} + \Delta K_y. \quad (13)$$

Then the phase function through the modified SM is rearranged into

$$\phi_{nsq}^{MSM}(K_r, K_x) = -\Delta K_y \cdot r - \sqrt{K_{rc}^2 - K_x^2} \cdot r - K_x \cdot x. \quad (14)$$

The first exponential term in (14) is a linear term corresponding to the range position of target. Clearly, the modified SM resolves the range and azimuth wavenumber coupling, namely, corrects the RCM. And the second term depends only on the azimuth wavenumber and r, but no longer couples with the range wavenumber. Together with the last azimuth linear phase, the second term corresponds to the final azimuth focusing. Since RCM is eliminated, followed range IFT processing can discriminate targets at different range into different range cells. And azimuth IFT is applied to transfer the signal into slow time domain, where the extension of the target response in slow time corresponds exactly to its extension in the raw data. Therefore, precise MoCo can be applied at this step, if accurate motion error information is available. After MoCo in this step, range-dependent matched filtering is used to compensate the second term in (14) and achieve a well-focused image. In contrast to the standard *Omega-k* algorithm, EOK separates the RCM and azimuth focusing into two independent steps, and thus precise MoCo can be performed on the slow-time signal after RCM correction. Due to the coarse MoCo via navigation measurements before performing EOK, and the residual motion error usually represents phase error only and the range error is usually constrained within one range cell. This assumption is generally valid in broadside SAR, since correction of RCM caused by motion error is corresponding to range cell in the scale of meters or decimeters, while the compensation of phase error is corresponding to the wavelength in the scale of centimeters or decimeters. In this sense, the coarse MoCo is usually accurate enough to remove the range error and only the phase error should be accounted in the MoCo after RCM correction. In the next section, we will see that this assumption is only valid in the non-squinted case, rather than in the highly squinted SAR imaging.

Based on the squinted PTRS expression in (9), EOK is easily extended to the squinted SAR mode, and a modified SM is designed as

$$\sqrt{K_r^2 - K_x^2}\cos\varphi \to \Delta K_y + \sqrt{K_{rc}^2 - K_x^2}\cos\varphi. \quad (15)$$

Then, the phase function in (10) becomes

$$\begin{aligned}\phi_{sq}^{MSM}(K_r,K_x)&=-\Delta K_y\cdot r-\sqrt{K_{rc}^2-K_x^2}\\&\quad\times\cos\varphi\cdot r-K_x\cdot(r\sin\varphi+x).\end{aligned}\tag{16}$$

Similar to the non-squinted mode, the coupling term between range and azimuth wavenumbers is resolved, correcting the RCM effectively. The second term corresponds to the azimuth focusing term and the last term corresponds to the final azimuth position of target in the image. Then, by applying range IFT to obtain range compression and azimuth IFT to transfer the signal back into the slow-time domain. And time-domain MoCo should be performed in this stage. At last, azimuth matched filtering is performed to achieve high resolution image. It seems that application of the squinted *Omega-k* for focusing highly squinted SAR data is straightforward. However, direct application of the squinted *Omega-k* to UAV-SAR imagery encounters inherent difficulties. Due to the lack of precision of navigation system, significant motion error is rest after MoCo via the recorded motion measurements. Therefore, data-driven autofocus approaches are usually necessary to compensate the residual motion error. This processing is deemed to be consistent with the squinted *Omega-k* algorithm. In the following section, an autofocus approach is developed for highly squinted UAV-SAR based on the motion error analysis.

III. Motion Error Analysis and Squinted Phase Gradient Autofocus

A. Effects of the Modified SM on Motion Errors

In this section, we introduce the residual motion error into the signal model and analyze the effect of the modified SM in (15) on it. Considering the residual motion error after coarse compensation by using the INS/IMU measurements, the slant range expression in (1) is shifted into

$$\tilde{R}(X)=R(X)+\Delta R_{err}(X)\tag{17}$$

where $\Delta R_{err}(X)$ denotes the residual motion error. For generality, the residual range error is extended into a polynomial function as

$$\Delta R_{err}(X)=e_2X^2+e_3X^3+e_4X^4+\cdots\tag{18}$$

where e_k denotes the k-th order coefficient, which is generally dependent on the range and azimuth position of the target. Note that, in (18) the first-order term is not accounted. Because the first-order term in range error induces additional Doppler shift and range walk, namely, it equivalently causes the squint angle change. Therefore, the effect can be compensated by Doppler centriod estimation [14], [15] corresponding to the squint angle estimation.

For simplicity, only exponential terms of received signal is considered in the following deduction. After range matched filtering, the received signal expression in (4) is rewritten as

$$\begin{aligned}S_{MF}(K_r,X)&=\exp\left[-jK_r\cdot\sqrt{(r\cos\varphi)^2+(X-x-r\sin\varphi)^2}\right]\\&\quad\times\exp\left[-jK_r\cdot\Delta R_{err}(X)\right].\end{aligned}\tag{19}$$

Then, azimuth FT is applied to achieve the PTRS corresponding to the processing in (6), which gives

$$\begin{aligned}S_{MF}(K_r,K_x)&=\int S_{MF}(K_r,X)\ \exp(-jK_xX)dX\\&=\int\exp\left[-jK_r\cdot\sqrt{(r\cos\varphi)^2+(X-x-r\sin\varphi)^2}\right]\\&\quad\times\exp\left[-jK_r\cdot\Delta R_{err}(X)\right]\cdot\exp(-jK_xX)\,dX.\end{aligned}\tag{20}$$

According to the POSP, the first derivative of the phase function with respect to X in (6) is set to zero as

$$\begin{aligned}K_r\frac{(X-x-r\sin\varphi)}{\sqrt{(r\cos\varphi)^2+(X-x-r\sin\varphi)^2}}\\+K_r\cdot\frac{\partial\Delta R_{err}(X)}{\partial X}+K_x=0.\end{aligned}\tag{21}$$

Due to the lack of information about the range error, it is impossible to solve the equation perfectly. Herein, we introduce an approximation to obtain the stationary point. Generally, the residual range error after coarse MoCo is nominal compared with the range history $R(X)$. In this sense, the residual phase error is nominal compared with the phase history of the PTRS. Therefore, we can use the PTRS phase to determine the stationary point and neglect the effect from the phase error. Generally, the difference between the stationary points in (7) and (20) is very small. This assumption simplifies the derivation of the stationary point, and it is usually valid in our MoCo. It will be presented in next subsection that, in our MoCo scheme, we adapt the overlapping sub-aperture processing. During a short sub-aperture data, the motion error is usually very small and manifests low-order characteristics, which ensures high accuracy of above assumption. Furthermore, the MoCo is implemented by an iterative correction procedure, which overcomes motion error stage by stage. Therefore, even if the motion error is large in the first iterations, it will be small enough without affecting the stationary point approximation after several iterations. Therefore, a rigid solution to (21) is X^* given in (8). By substituting (8) into (19), we obtain the expression of PTRS

$$\begin{aligned}&S_{MF}(K_r,K_x)\\&=\exp\left\{-j\left[\left(\sqrt{K_r^2-K_x^2}\cos\varphi+K_x\sin\varphi\right)\cdot r+K_x\cdot x\right]\right\}\\&\quad\times\exp\left[-jK_r\cdot\Delta R_{err}(X^*)\right].\end{aligned}\tag{22}$$

Then, by applying the modified SM and subsitituting (15) into (22), we have

$$\begin{aligned} &S_{MF}^{MSM}(\Delta K_y, K_x) \\ &= \exp\left\{-j\left[\Delta K_y r + \sqrt{K_{rc}^2 - K_x^2}\cos\varphi \cdot r + K_x\left(r\sin\varphi + x\right)\right]\right\} \\ &\quad \times \exp\left[-j\vartheta\left(\Delta K_y, K_x\right)\right] \end{aligned} \tag{23}$$

where

$$\vartheta\left(\Delta K_y, K_x\right) = \sqrt{\left(\frac{\Delta K_y}{\cos\varphi} + \sqrt{K_{rc}^2 - K_x^2}\right)^2 + K_x^2} \cdot R_{err}\left(X^*\right) \tag{24}$$

and $\Delta R_{err}\left(X^*\right) = e_2(X^*)^2 + e_3(X^*)^3 + e_4(X^*)^4 + \cdots$. From (8), we note that X^* is a function of both K_r and K_x, and thus, after the modified SM, X^* is a function of ΔK_y and K_x. Then, azimuth IFT is applied to transfer signal back into the slow-time domain, which yields

$$\begin{aligned} &S_{MF}^{MSM}(\Delta K_y, X) \\ &= \int S_{MF}^{MSM}(\Delta K_y, K_x)\ \exp\left(jK_x X\right) dX \\ &= \int \exp\left\{-j\left[\Delta K_y r + \sqrt{K_{rc}^2 - K_x^2}\cos\varphi \cdot r + K_x(r\sin\varphi + x)\right]\right\} \\ &\quad \times \exp\left[-j\vartheta\left(\Delta K_y, K_x\right)\right] \cdot \exp\left(jK_x X\right) dK_x. \end{aligned} \tag{25}$$

In order to obtain the analytic expression of $S_{MF}^{MSM}(\Delta K_y, X)$, we use the POSP and have

$$-\frac{K_x}{\sqrt{K_{rc}^2 - K_x^2}}\cos\varphi \cdot r - r\sin\varphi - x - \frac{\partial\vartheta\left(\Delta K_y, K_x\right)}{\partial K_x} + X = 0. \tag{26}$$

Due to the small value of the error term, we neglect its contribution in to the stationary point calculation and get

$$-\frac{K_x}{\sqrt{K_{rc}^2 - K_x^2}}\cos\varphi \cdot r - r\sin\varphi - x + X \approx 0. \tag{27}$$

The approximate stationary phase point is

$$K_x^* \approx -K_{rc}\frac{\left(X - r\sin\varphi - x\right)}{\sqrt{\left(\cos\varphi \cdot r\right)^2 + \left(X - r\sin\varphi - x\right)^2}}. \tag{28}$$

By Substituting (28) into (25), we have the spectrum that

$$\begin{aligned} &S_{MF}^{MSM}(\Delta K_y, X) \\ &= \exp\left\{-j\left[\Delta K_y r + K_{rc}\sqrt{\left(\cos\varphi \cdot r\right)^2 + \left(X - r\sin\varphi - x\right)^2}\right]\right\} \\ &\quad \times \exp\left[-j\vartheta\left(\Delta K_y, K_x^*\right)\right]. \end{aligned} \tag{29}$$

And substituting (28) into (8) leads to

$$X^*\left(K_x^*\right) = X. \tag{30}$$

Extending $\vartheta\left(\Delta K_y, K_x^*\right)$ into first-order Taylor series at $\Delta K_y = 0$, we have

$$\begin{aligned} &\vartheta\left(\Delta K_y, K_x^*\right) \\ &\approx \vartheta\left(\Delta K_y, K_x^*\right)|_{\Delta K_y = 0} + \left.\frac{\vartheta\left(\Delta K_y, K_x^*\right)}{\partial \Delta K_y}\right|_{\Delta K_y = 0} \times \Delta K_y \\ &= K_{rc} \cdot \Delta R_{err}\left(X\right) + \Delta K_y \times \Delta R'_{err}\left(X\right) \end{aligned} \tag{31}$$

where

$$\begin{aligned} &\Delta R'_{err}\left(X\right) \\ &\quad = \Delta R_{err}\left(X\right) + \frac{r\sin\varphi}{\cos^2\varphi} \cdot \left(2e_2 X + 3e_3 X^2 + 4e_4 X^3 \cdots\right). \end{aligned} \tag{32}$$

Detailed deduction about above expression can be found in Appendix A. In (31), the first term represents the phase error in the slow-time domain, which is only related to $\Delta R_{err}\left(X\right)$, in other words, the squinted SM does not change variance and characteristics of the phase error. This consistency of phase error before and after SM is also the base that the MoCo can be successfully used in the non-squinted SAR mode in [8]. The second term is a linear function of ΔK_y, corresponding to the range error. From (32), one can notice that the range error is composed by two terms: the first corresponds to $\Delta R_{err}\left(X\right)$ consistent to the phase error, and the second term is induced by the modified SM. And with the increase of squint angle, the second term becomes pronounced. We call this phenomenon as the inconsistence of phase error and range error from the modified SM. Applying IFT with respect to ΔK_y and omitting the constants introduced, we achieve the range compressed signal as

$$\begin{aligned} &s_{MF}^{MSM}(y, X) \\ &\quad = \mathrm{sinc}\left[B \cdot \left(y - r - \Delta R'_{err}\left(X\right)\right)\right] \\ &\qquad \times \exp\left[-jK_{rc}\sqrt{\left(\cos\varphi \cdot r\right)^2 + \left(X - r\sin\varphi - x\right)^2}\right] \\ &\qquad \times \exp\left[-jK_{rc} \cdot \Delta R_{err}\left(X\right)\right] \end{aligned} \tag{33}$$

where y denotes the range coordinate with respect to ΔK_y and B is the bandwidth corresponding to ΔK_y. In this stage, the motion error is expected to be corrected precisely. In conventional MoCo of airborne SAR applications, the majority of motion errors are compensated on raw data via navigation measurements and the residual motion error is usually nominal causing no range error. Then, in this stage, the fine MoCo is performed on the RCM corrected signal [3], [8]. However, in coping with highly squinted SAR data with the modified EOK, the RCM error is not only introduced by residual motion error, but also the modified SM. When and only when $\varphi = 0$, the range error in (32) equals to $\Delta R_{err}\left(X\right)$. Otherwise, we usually have $\Delta R'_{err}\left(X\right) \gg \Delta R_{err}\left(X\right)$. For clarity, we set a numerical example to explain the effect of SM on range error. Taking $r = 30$ km, $\varphi = 50°$ and X changes from -1000 to 1000 meters, the residual range error is assumed as a five-order polynomial function shown in Fig. 2(a), and the corresponding RCM error is given in Fig. 2(b). In Fig. 2(a), we note $\Delta R_{err}\left(X\right)$ varies within only several centimeters. However, due to the large value of r, the corresponding $\Delta R'_{err}\left(X\right)$ is magnified up to several meters after the modified SM, which surely exceeds one resolution cell bringing additional range cell migration. In other words, even very small range error is rested after coarse MoCo, serious range cell migration presents after the SM in highly squinted SAR imagery. In this sense, the requirement of accuracy of MoCo is usually beyond the capability of INS/IMU systems in conventional airborne SAR, saying nothing of UAV-SAR applications. Therefore, serious

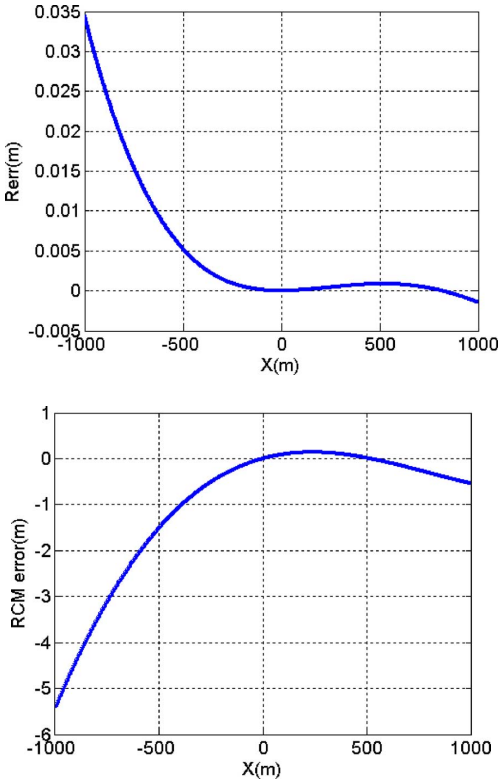

Fig. 2. (a) Residual range error. (b) Range error after modified SM.

RCM error and considerable phase error certainly exist in the range compressed signal. For our issue of highly squinted UAV-SAR imagery with the squinted *Omega-k* algorithm, high precise autofocus approach is necessary to generate high quality image.

B. Squinted Phase Gradient Autofocus (SPGA)

In this subsection, we focus on precise autofocusing for the highly squinted UAV-SAR imagery based on an improved PGA, named by squinted phase gradient autofocus (SPGA) algorithm. Before presenting our approach, let us review the standard PGA briefly, which forms the basis of SPGA. PGA [23] is one of the most useful autofocus algorithms in airborne SAR imagery, which has been widely applied in various SAR applications, particularly in spotlight mode SAR imagery. The PGA provides robust performance over wide variety of scene contents due to its robustness to strong clutter and noise interference. In application of PGA to SAR imagery, the RCM and high order azimuth phase are removed. And in the EOK case, the azimuth deramping [1], [13], [24] is first applied to remove the quadratic term after the modified SM and transferring data in the range-compressed and azimuth slow time domain before performing PGA. In general, PGA is implemented by five sequenced steps as follows.

1) Range Cells Selection: Generally, motion error usually represents spatial-invariant (or weakly spatial-variant) characteristics in the recorded data. And PGA exploits the redundancy of the phase error information upon different range cells. However, there is no need to use all range bins to extract the phase error. And, selecting proper samples makes the estimation more efficient without losing precision. Range bins containing prominent scatterers are good candidates for PGA estimation. It is not difficult to understand that the more proper samples we have, the more efficient and precise PGA is. Adapting this idea, the QPGA improves PGA based on the fact that a single range cell usually contains more than one dominant scatters [25]. QPGA also suggested that the signal-to-clutter ratio (SCR) criteria rather than the original energy criteria for choosing targets can improve the estimate of phase gradient.

2) Circular Shifting: Azimuth FT is first applied to the selected range cells to generate a coarse focused image, and the azimuth cell with the strongest response is circularly shifted to the image center for each range cell, which removes the offset in the Doppler domain due to the azimuth position of the target. Alignment of the strongest azimuth bins improves the SCR for the phase gradient estimation by subsequent windowing processing.

3) Windowing: The next step is windowing the circularly shifted imagery. Windowing preserves the width of the dominant blur of the target while discarding clutter with negative contribution to the phase gradient estimation. In this step the selection of the window size is usually significant to the PGA performance. In general, it is estimated by incoherent summing over the range bins to obtain a one-dimensional extended response and then using an energy-threshold to determine the window width. Also, a pre-determined decreasing window width works quite well in reality.

4) Error Phase Gradient Estimate: After circular shifting and windowing, the phase gradient is ready to be estimated. The linear unbiased minimum variation (LUMV) and the maximum likelihood (ML) phase-gradient-estimation kernel have been given in [23]. Following the idea of weighted-least square estimation in [26], a weighted ML kernel is given in [24]. Weights adjust the contribution of different samples to phase gradient estimate according to the SCR, which are designed to encourage the contribution of high SCR samples and discourage those with low SCR. And the selection of samples can be much relaxed and fast convergence can be obtained. Using symbol $u(k,h)$ to denote the discrete bin of the circular shifted and windowed samples at (k,h) in the range compressed and slow time domain. The weighted maximum likelihood (WML) kernel for the phase gradient estimate is given by

$$\hat{\dot{\vartheta}}_{err}^{\mathrm{WML}}(h) = \arg \sum_{k=1}^{K} \frac{w_k \cdot [\mathrm{conj}\,[u(k,h)] \cdot u(k,h+1)]}{\sum_{j=1}^{K} w_j} \tag{34}$$

where $\hat{\dot{\vartheta}}_{err}^{\mathrm{WML}}$ denotes the phase gradient estimate with WML kernel. w_k and w_j are the weights in the k-th and j-th range bins. The weight w_k for the k-th range bin is the inverse of the phase variance of the range bin. Detailed derivation of SCR estimation can be found in [24], [26]. In this paper, the proposed squinted PGA is implemented by WML kernel.

5) Iterative Phase Correction: The phase gradient $\hat{\dot{\vartheta}}_{err}^{\mathrm{WML}}$ is integrated to get the estimate of phase error and any bias and linear component is removed prior to performing correction to the signal. And the estimation and compensation process is repeated iteratively. As the image trends to be focused, the individual target becomes more compact, the SCR is improved, the

circular shifting and windowing are more precise and narrow, and the convergence is achieved.

SPGA also follows the five-step processing and retrieves the phase error iteratively. At first, we select all range cells of the range compressed signal above a pre-determined SCR threshold. Then each range cell is deramped to remove the quadratic phase. The reference phase function of the range cell corresponding to y is given by

$$Ref\,(X) = \exp\left[j \cdot K_{rc} R_0\,(X)\right] \tag{35}$$

where $R_0\,(X) = \sqrt{(y\cos\theta)^2 + (X - y\sin\theta)^2}$ corresponds to the range history of the center at equivalent range line corresponding to y. After deramping, we obtain

$$\begin{aligned} &s_{PGA}(y, X) \\ &= s_{MF}^{MSM}(y, X) \times Rref\,(X) \\ &= \exp\left\{-jK_{rc}\left[R\,(X) - R_0\,(X)\right]\right\} \cdot \exp\left[-jK_{rc} \cdot \Delta R_{err}\,(X)\right] \\ &= \exp\left\{-jK_{rc}\left[E\,(X; r, x) \cdot x + F\,(X; r, x) \cdot x^2\right]\right\} \\ &\quad \times \exp\left[-jK_{rc} \cdot \Delta R_{err}\,(X)\right] \end{aligned} \tag{36}$$

where

$$E\,(X; r, x) = -\frac{(X - r\sin\theta)}{\sqrt{(r\cos\theta)^2 + (X - r\sin\theta)^2}} \tag{37a}$$

$$F\,(X; r, x) = \frac{(r\cos\theta)^2}{2\sqrt[3]{(r\cos\theta)^2 + (X - r\sin\theta)^2}}. \tag{38b}$$

According to the derivation in Appendix B, we have the approximate expression of the deramped signal as

$$\begin{aligned} &s_{PGA}(y, X) \\ &\approx \exp\left\{-jK_{rc}\left[\alpha_0\,(r, x) + \alpha_1\,(r, x) \cdot X + \alpha_2\,(r, x) \cdot X^2\right]\right\} \\ &\quad \times \exp\left[-jK_{rc} \cdot \Delta R_{err}\,(X)\right] \end{aligned} \tag{39}$$

where $\alpha_0\,(r, x)$

$$\alpha_0\,(r, x) = -\sin\varphi \cdot x + \frac{\cos^2\varphi}{2r} \cdot x^2, \tag{40a}$$

$$\alpha_1\,(r, x) = -\frac{\cos^2\varphi}{r}x + \frac{3\sin\varphi\cos^2\varphi}{2r^2}x^2, \tag{40b}$$

$$\alpha_2\,(r, x) = \frac{3\left(\sin\varphi + \sin^3\varphi\right)}{2r^2}x. \tag{40c}$$

$\alpha_0\,(r, x)$ and $\alpha_1\,(r, x)$ correspond to the constant phase term and the linear phase terms, respectively. And $\alpha_2\,(r, x)$ is the coefficient related to the residual quadratic phase after deramping. In the case of non-squinted SAR case, the quadratic coefficient equals to zero and $\alpha_1\,(r, x) = -x/r$. Regardless of the approximation of (39), the only high order phase terms are corresponding to the motion error $\Delta R_{err}\,(X)$, and thus PGA can be directly utilized to extract the phase function induced by motion error. However, it is not the case when squint angle is not equal to zero as $\alpha_2\,(r, x) \neq 0$ anymore. And with the increase of squint angle, the quadratic phase term becomes significant to degrade the estimate of motion error. In this sense, the quadratic phase term corresponding to $\alpha_2\,(r, x)$ should be compensated before implementing PGA to estimate the motion phase error. Fortunately, $\alpha_2\,(r, x)$ is a linear function of the target azimuth coordinate and the residual quadratic phase is azimuth-dependent, and thus we can determine the residual quadratic phase by using the azimuth position of the target. Clearly, in the circular shifting step of the standard PGA, azimuth FT is applied to the range cell in (39) yielding a coarse focused image, and the majority of energy of the target is constrained around the azimuth wavenumber bin corresponding to

$$K_{ac} = \frac{4\pi}{\lambda}\alpha_1\,(r, x). \tag{41}$$

From K_{ac}, we can retrieve the azimuth position of the target. Substituting (40b) and (40c) into (41), we have a quadratic equation of x, which gives

$$\frac{K_{ac}\lambda}{4\pi} = -\frac{\cos^2\varphi}{r}x + \frac{3\sin\varphi\cos^2\varphi}{2r^2}x^2. \tag{42}$$

By solving the equation in (42), we obtain the estimation of the azimuth position of the target as follows.

$$x' = -\frac{r}{3\sin\varphi} - \sqrt{\frac{K_{ac}\lambda r^2}{6\pi\sin\varphi\cos^2\varphi} + \left(\frac{\cos^2\varphi r}{3\sin\varphi\cos^2\varphi}\right)^2}. \tag{43}$$

Therefore, the residual quadratic phase correction can be implemented by multiplying the phase function in (44) and deramped signal in (39) in slow time domain.

$$P_c(X) = \exp\left[j \cdot K_{rc}\alpha_2\,(r, x')\,X^2\right]. \tag{44}$$

In the circular shifting step of each SPGA iteration, above residual quadratic phase correction is performed for each sample scatterer.

In highly squinted SAR mode, the deramping can not remove all quadratic phase of phase function of a target. And the residual quadratic phase will be treated as phase error in PGA estimate. SPGA, as an extension of PGA, considers the residual quadratic phase ensuring the precise estimate of phase error. The estimation and compensation of the residual quadratic phase is embedded into the conventional PGA procedure. Therefore, high quality phase gradient estimate is ensured by the WML kernel. However, another notable difficulty of phase error retrieve in the squinted SAR imagery via the squinted *Omega-k* algorithm, is the residual range error after the modified SM we discussed in last subsection. We note that even very small range error brings considerable range error after the modified SM processing, which surely reduces the precision of phase error estimation through PGA. However, we can perform PGA to the deramped data with a lower resolution by the under-sampling process. The under-sampling process [27] eliminates the residual RCM directly by summing up N neighboring range cells into one single cell and $1/N$ is defined as the under-sampling ratio. Also under-sampling process can be implemented by extracting only part of frequency band data to obtain a range-compressed data block, which inherently has an energy loss of the signal. Therefore, summing scheme should be proper to reduce the RCM effect on the SPGA.

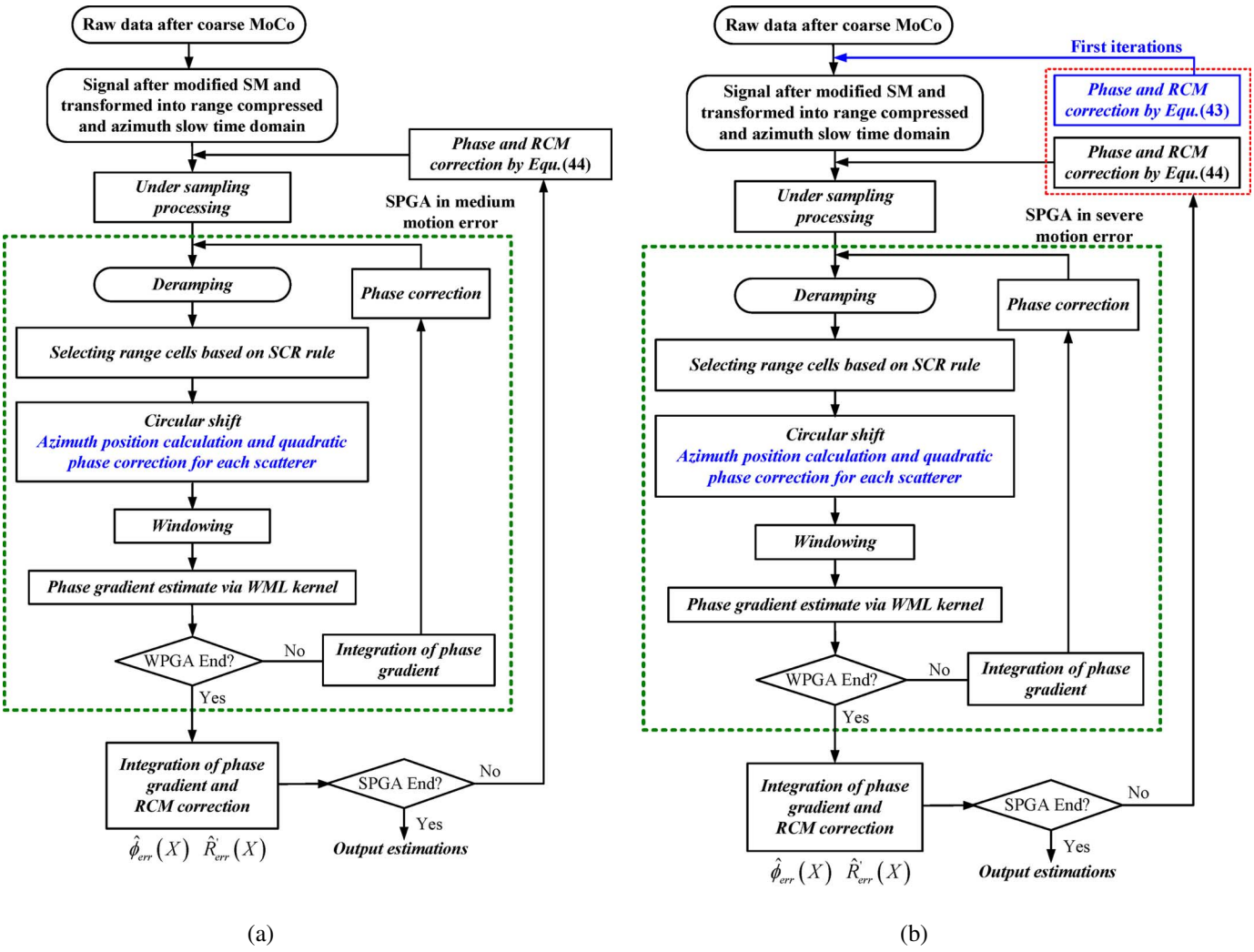

Fig. 3. (a) Flowchart of the SPGA for medium motion error. (b) Flowchart of the SPGA for severe motion error

As one notes in (33), the residual phase error are directly related to $\Delta R_{err}(X)$, and therefore we can have the estimate of residual motion error by

$$\Delta\hat{R}_{err}(X) = \frac{\hat{\vartheta}_{err}^{\mathrm{WML}}(X)}{K_{rc}} \tag{45}$$

where $\hat{\vartheta}_{err}^{\mathrm{WML}}(X)$ is the integrated phase error from WPGA estimate. With the estimate of range error, we can perform the fine MoCo in the raw data, and the modified SM follows. Due to correction of $\Delta\hat{R}_{err}(X)$, the residual errors would be lessening. An iteration procedure can be utilized to correct the entire range error effectively. This kind of iteration can be also found in [16], [24]. However, it is usually with low efficiency because the time-consuming SM interpolation is performed in each iteration. Actually, in (32) we can find that the relation between the amplified RCM and range error is certain, and direct estimate of RCM from the $\Delta\hat{R}_{err}(X)$ is possible. Then, correction of both phase and RCM errors can be performed to the mapped data rather than raw data, which can improve the efficiency dramatically. In terms for calculating RCM error after the modified SM, sequentially, $\Delta\hat{R}_{err}(X)$ is fitted into low-order polynomial function and we obtain the estimates of coefficients as $\hat{e}_2$, $\hat{e}_3$, $\hat{e}_4$ and so on. Then, the RCM error after modified SM is estimated by

$$\Delta\hat{R}'_{err}(X) = \Delta\hat{R}_{err}(X) + \frac{r\sin\varphi}{\cos^2\varphi}\cdot\left(2\hat{e}_2X + 3\hat{e}_3X^2 + 4\hat{e}_4X^3\cdots\right). \tag{46}$$

Due to clutter and RCM errors, the estimated range error is deemed to be contaminated by noise in some degree, which takes the risk of inaccuracy in polynomial function fitting, especially the high order coefficients and consequently causes unacceptable error in RCM calculation. For robust correction, we use a stage-wise scheme by decreasing the number N in under-sampling iteratively. In the first several iterations, due to severe range error, N with large value (eight for instance), is utilized. And low order polynomial fitting, such as three or four orders, is used to get a coarse estimation of motion error. Then both phase and range error are reduced to a small degree before we start the next iteration, and therefore in this iteration, we can choose a smaller N and higher order polynomial fitting to get fine estimation of both phase and range error. Generally, precise estimation can be achieved within only several iterations. For clarity, the flowchart of the SPGA is shown in Fig. 3(a). However, in presence of severe motion error even after coarse MoCo

by using navigation data, the phase error estimate degrades due to very severe range error occurs after the modified SM. As a result, the range error calculation via (46) loses its accuracy dramatically, which will not ensure accurate correction. In this case, we should perform the MoCo on the raw data rather than on that after the modified SM. By removal of phase and range errors in the raw data, then the residual error is decreased to a low level. Then the *Omega-k* algorithm is applied, and nominal range and phase errors are presented in the mapped data. Then we perform the SPGA subsequently giving an optimal compensation. This scheme is certainly of high computational load, because we have to perform the SM interpolation more than once. But it enables the SPGA cope with very severe motion error in real highly squinted UAV-SAR imagery. And hybrid of the corrections before and after SM is direct: correction on the raw data in the first several iterations, and then correction on data after SM in the last iterations, which can make a tradeoff between the precision and computational complexity. The procedure of SPGA in dealing with severe motion error is shown in Fig. 3(b). In summary, SPGA outperforms the standard PGA in focusing squinted SAR data from two aspects: 1) SPGA considers the residual quadratic phase terms after deramping operation, which avoids severe error in the phase gradient estimation; 2) The non-systematic RCM induced by both motion error and the SM processing is overcome in SPGA.

The SPGA is ready to autofocus the highly squinted spotlight SAR image. However, its extension to squinted stripmap UAV-SAR imagery requires some necessary modifications. In general, PGA frameworks cannot be directly applied to stripmap SAR imagery and SPGA is not an exception. However, for the UAV-SAR application, stripmap mode should be one of the most essential operating modes. In the stripmap mode the aperture positions of different sactterers displace with each other within the whole coherent processing interval. Applying the PGA approaches to the stripmap mode brings an inherent problem stemming from overlapping apertures of different scatterers, which span different segments of the phase gradient estimate with potentially different local linear components, will not always give the same phase gradient in the overlapped region [28]. And thus difference of local linear components from different targets inherently introduces incoherence between phase gradient estimation leading to the failure of PGA approaches. To overcome this problem in utilization of PGA schemes in the stripmap SAR imagery, a simple but useful scheme is proposed in [29], which shifts signal of the stripmap SAR into spotlight representation by splitting it into small azimuth blocks and estimating the error phase gradient for each segment independently. Then the segmental phase gradients are integrated into segmental phase error functions, and coherent connection is performed to combine them into the full aperture function. In our SPGA with the sub-aperture process, overlapping is applied to extract the information about discontinuities between two joint sub-aperture phase error segments. The overlapping segments also provide overlapping phase error estimates of azimuth blocks, which are illustrated in Fig. 4. The linear phase differences can be easily extracted from the overlapping sub-aperture phase functions. In real application, the overlapping part can be selected as a quarter or half of a sub-aperture. And the global linear phase term

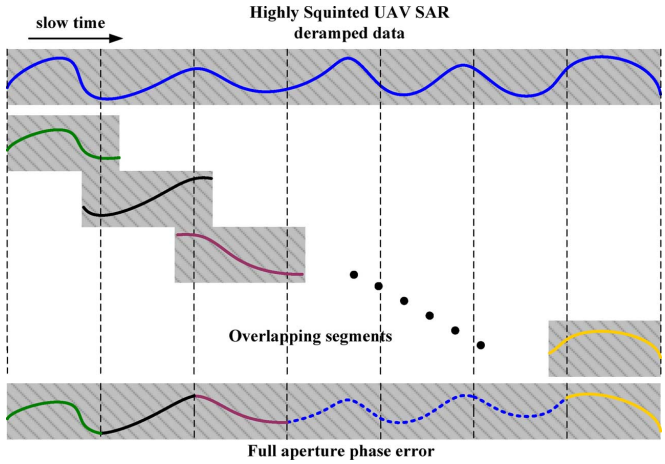

Fig. 4. Full aperture phase error combination.

is removed from the full-aperture phase error function. And then, range error is retrieved from the phase error function. And phase error and range error are estimated and corrected iteratively until an optimal convergence.

Another difficulty encountered in the stripmap UAV-SAR autofocus is the spatial-variance of motion error. In stripmap mode, radar beam usually covers a much wider scene than the spotlight SAR does, especially in the low attitude angle case. The SPGA assumes the radar beam is narrow enough that the motion error represents spatial-invariance. However, in UAV-SAR operating at stripmap mode, this assumption may be not rigid enough. When accounting the range-dependence of phase error, range blocking is utilized to ensure application of the SPGA. And the range blocks should be small enough that the spatial variance of phase error within can be regarded as non-spatial variant case. Contrasting to range blocking process, the phase-weighted-estimation PGA (PWE-PGA) [23] provides an estimation kernel for computing the phase gradients with a range-variant model. Since its model is based on non-squinted SAR geometry, PWE-PGA can't be directly extended into SPGA. In our case of phase and range error correction with SPGA, we use the range blocking in estimation and the compensation is independently applied for each block. Consequently, well-focused image of high squinted SAR can be obtained by the azimuth matched-filtering in the EOK processing for each block. And range block images are fused to achieve the full-scene SAR image. A useful procedure of SPGA in deal with highly squinted stripmap UAV SAR imagery is given in Fig. 5. And the extension of the MoCo procedure to deal with severe motion error is presented in Fig. 3(b).

IV. Real Data Experiments

In the following, we give the experimental results of UAV SAR imagery via the presented squinted *Omega-k* algorithm and SPGA-based MoCo. To illustrate the performance of the proposed method, two experiments are carried out by using data sets measured by an experimental SAR system. The first experiment is performed to validate the performance of the proposed autofocus scheme in highly squinted UAV-SAR imagery with medium motion error. And the second experiment is carried out to illustrate its performance under severe motion error. Both of the data sets are recorded in one plane sortie. The SAR works at

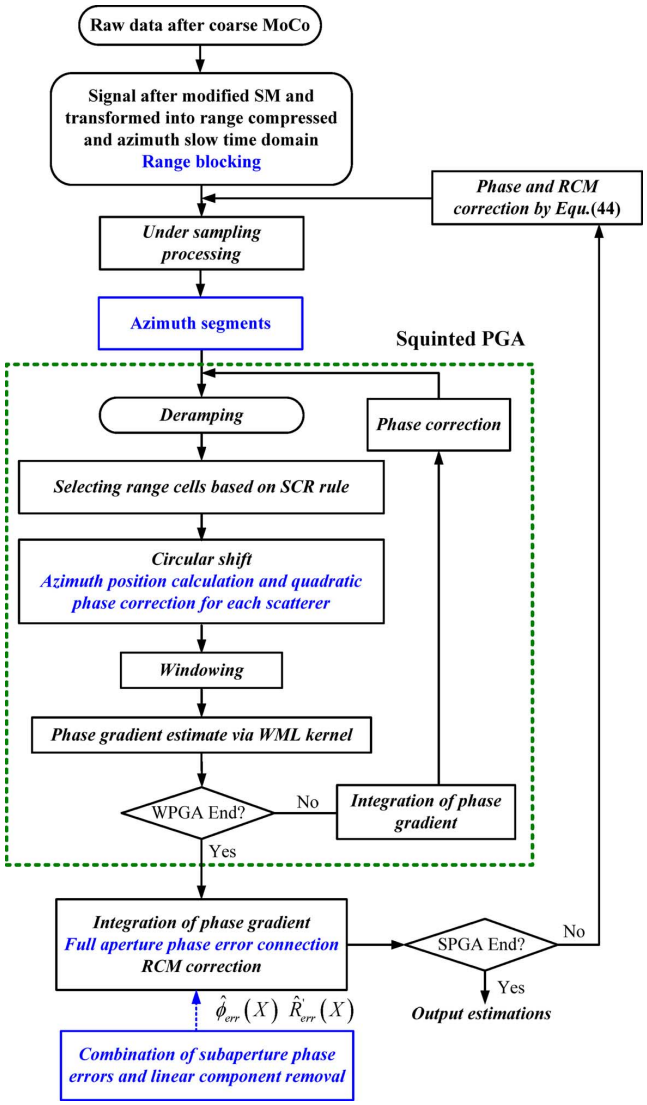

Fig. 5. Flowchart of the SPGA for stripmap UAV-SAR.

X-band in squint stripmap mode and it provides resolution about 2.15 m × 2.15 m (range × azimuth). It transmits a pulsed waveform, with pulse duration of 10 us and bandwidth of 70 MHz, and the beam width is about 1.2 degrees. During the data collection, the squint angle is about 50 degrees and the flying velocity is about 60 m/s. The height of UAV is about 2800 m and the range central to the scene is 28.32 km. The SAR system is equipped with an inertial navigation system with medium accuracy. And the measured motion parameters by the system provide the trajectory deviation in the coarse MoCo and the rest motion error is expected to be corrected by the SPGA-based MoCo schemes. In the following experiments, one can notice that in the both cases of medium and severe motion error, the SPGA-based MoCo can precisely compensate the rest of motion errors, including phase and nonsystematic range migration error, and generate well-focused images.

A. Experiment With Medium Motion Error

In the data set utilized in this experiment, the motion error is not severe, as after coarse MoCo via the INS data, the image

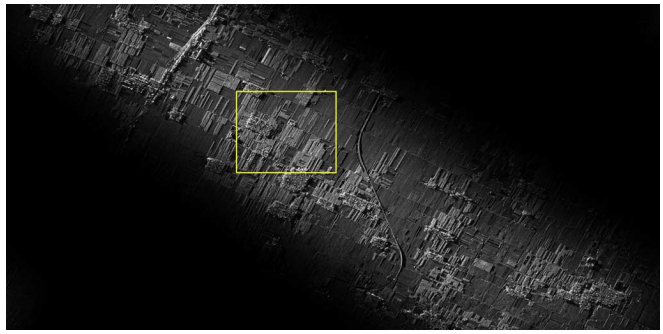

Fig. 6. Image with INS MoCo.

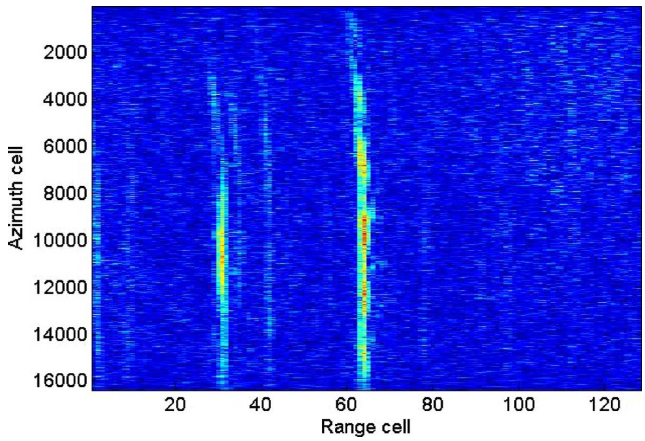

Fig. 7. Range profile of a dominant scatter with range error.

can be focused roughly, along with some degree of blurring and geometric distortion. The generated image via the squinted *Omega-k* algorithm with only coarse MoCo is shown in Fig. 6. The swath of image in range is about 7500 meters, and the process of geometric correction is done. The vertical direction is range and the horizontal direction is azimuth. The focusing quality in azimuth indicates that the residual phase error after the coarse MoCo is nominal, but distinctive range error is present in the data after the modified SM. For clarity, we extract the profile of a dominant target in the range-compressed and slow time domain, as shown in Fig. 7. From Fig. 7, one can clearly notice that distinctive range error exceeds over about four cells in the aperture interval, which certainly causes the degradation of focusing quality in the final image. The presence of RCM also indicates that residual motion error still exists in the data after MoCo with INS data. Then, the proposed SPGA is applied to the data set to estimate the residual phase error and range error subsequently. The data after SM is separated into 16 segments and each of them is performed by SPGA with WML kernel to retrieve the phase function, respectively. Then the functions are aligned into a full aperture function. In this data set the range-dependence of phase error is nominal, and thus we need no range blocking processing. For clarity, five iterations are utilized in the SPGA, and the phase errors corresponding to iterations are given in Fig. 8. During the iterations of SPGA, the phase error is optimized within -10 to 5 radians, which corresponds to range error at a scale of only several wavelengths. However, the corresponding RCM is amplified by the SM dramatically. We show the range

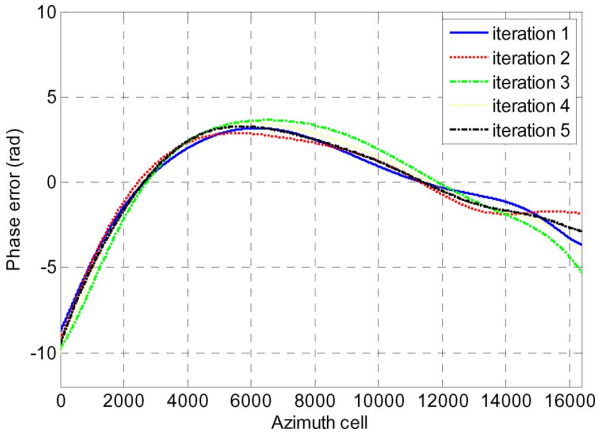

Fig. 8. Residual phase error estimated by the SPGA.

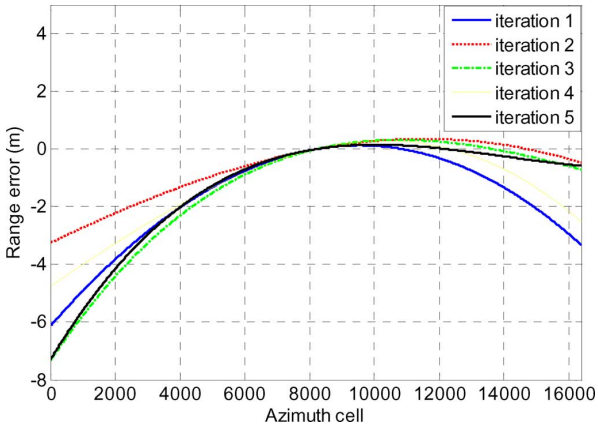

Fig. 9. RCM extracted from phase errors by (46).

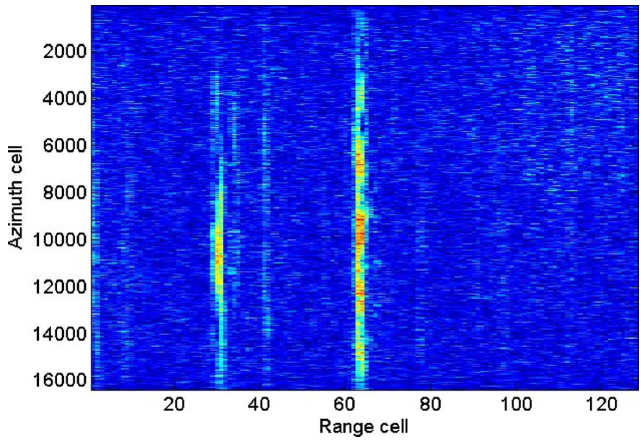

Fig. 10. Range profile of the dominant scatter after SPGA correction.

errors calculated by using (46) in Fig. 9, which change from -8 to 0 meters. Clearly, the standard PGA can not handle the range errors effectively. In this experiment, we perform range and phase correction directly on the signal after SM, rather than on the raw data. Fig. 10 gives the corrected profile of the dominant scatter, which shows that the range error is compensated effectively by using the estimate in Fig. 6. And the final generated image is shown in Fig. 11. For comparison, in Fig. 12(a) and (b), we show the magnified local images highlighted by the rectangles in Figs. 6 and 11, whose entropy is 13.303 and 13.291,

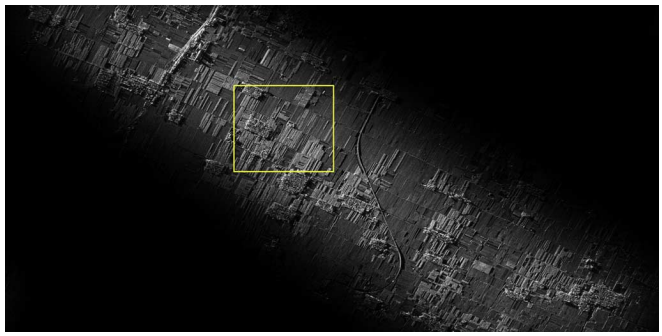

Fig. 11. Image with INS data and SPGA.

respectively . According to the entropy values, we notice that better focusing performance is achieved, as the residual phase and range errors are corrected by the SPGA-based MoCo.

B. Experiment With Severe Motion Error

Herein, we perform the experiment by using another data set, which contains severe motion error due to atmospheric turbulence. By using the INS data, the coarse MoCo is performed to remove the major of motion error. However, the residual errors are still severe enough to cause significant blurring, which can be noted from image obtained by the squinted *Omega-k* algorithm without SPGA in Fig. 13. Actually, the focusing degradation is mostly introduced by the RCM amplified by the SM processing. Therefore, the focusing performance will be not improved even the standard PGA is applied. As we can note from Fig. 14, the range shift exceeds over about ten cells, which surely brings serious blurring in the image. In this experiment, the residual motion error is distinctively larger than that in experiment A. Herein, and the residual motion error causes very serious range shift through the *Omega-k* algorithm. This severe range shift can cause precision degradation of the SPGA even we perform the sub-sampling processing. And inaccurate phase error estimate introduces unacceptable error in range error calculation via (46). Therefore, we need to perform the correction on the raw data rather than on that after SM processing following the flow in Fig. 3(b). Then, SPGA is used to the corrected the residual motion error. Generally, desired range correction can be achieved with only once correction on the raw data. It is not difficult to understand that although some estimate error is introduced due to the residual range error through SM processing, most motion error can be retrieved by the WPGA kernel. After range error correction on the raw data, most of RCM is corrected, which we can note from Fig. 16. Fig. 16 shows the profiles after only once phase and range correction on the raw data by using the SPGA estimated motion error. Then, the SPGA is performed again to correct the residual phase error and range shift on the data after SM directly. In this step, the procedure is identical to that we use in the experiment A. The estimated phase errors and corresponding range errors from the five iterations are shown in Figs. 17 and 18, respectively. The final focused image is given in Fig. 19. For comparison, the highlighted local image in Figs. 13 and 19 are amplified in Fig. 20(a) and (b), whose entropy is 12.983 and 1.958, respectively. Clearly, the improvement of image quality is obtained via the SPGA. As from Fig. 20(b), we can note the freeway, villages and wild

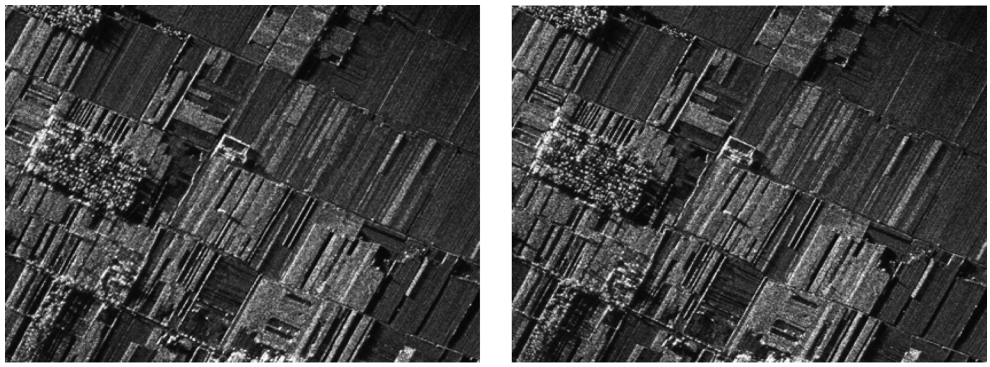

(a) (b)

Fig. 12. Image comparison. (a) Magnified local image from Fig. 6. (b) Magnified local image from Fig. 11.

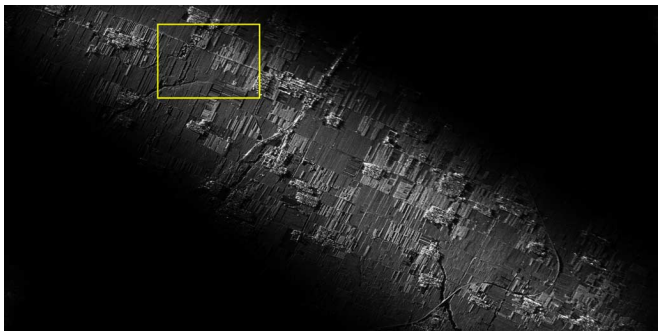

Fig. 13. Image with INS MoCo.

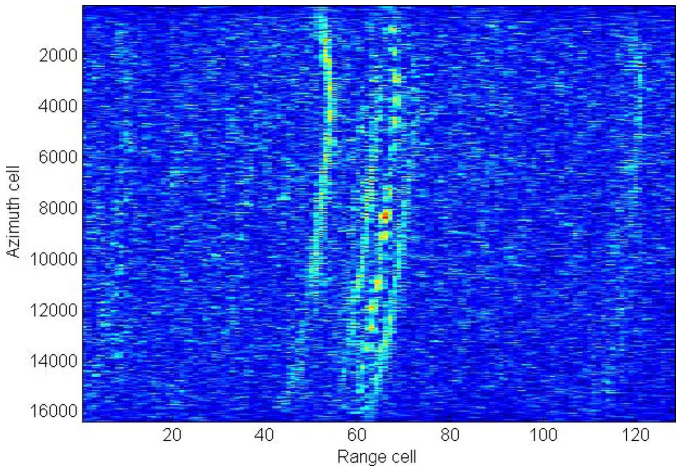

Fig. 14. Range profile of dominated scatterers.

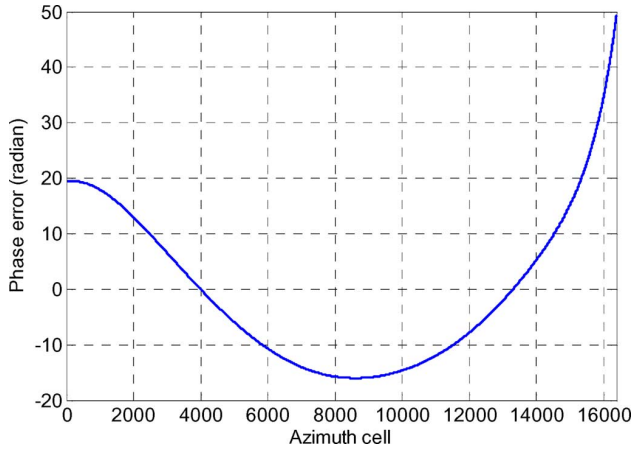

Fig. 15. Phase error estimated from the Stolt mapped data.

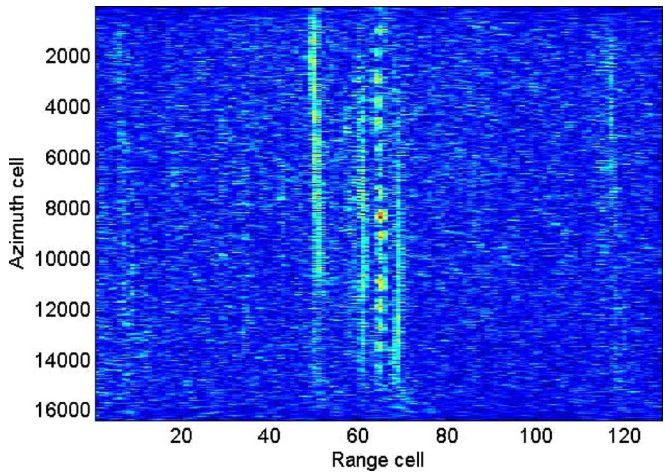

Fig. 16. Range profile of dominated scatterers after correction on the raw data.

scenes are clearly distinguished and well-focused with high contrast. The experiment confirms that our autofocus approach is potential in focusing UAV-SAR data with severe motion error with equipment of only a medium or low accuracy INS.

V. Conclusion

In this paper, a robust and efficient imaging and MoCo scheme for highly squinted UAV-SAR imagery is proposed. The inconsistence of phase error and range error in the squinted wavenumber-domain focusing is presented, which indicates that even the phase error is very small the range error would be magnified significantly by SM. Also a novel squinted phase gradient autofocus approach is proposed. In SPGA, the phase error and range error are estimated jointly via an iterative processing. High in precision and efficiency, the autofocus approach is potential in UAV-SAR operating with a large squint angle. Real-measured data is used to validate the proposed approach.

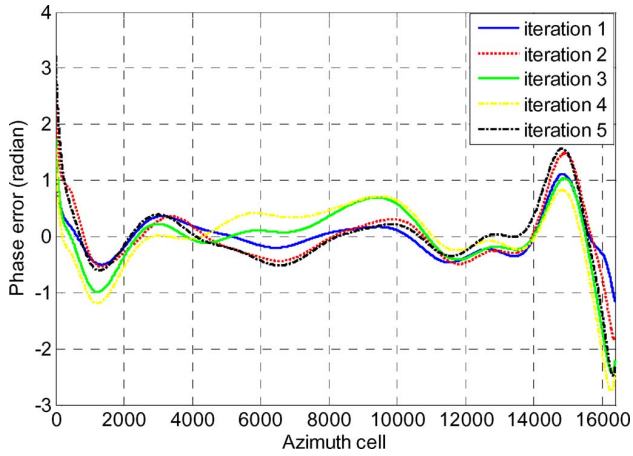

Fig. 17. Phase error from SPGA iteration.

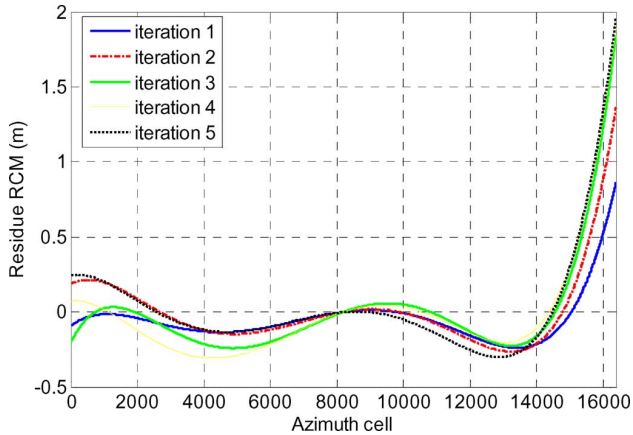

Fig. 18. Range errors extracted form phase errors by (46).

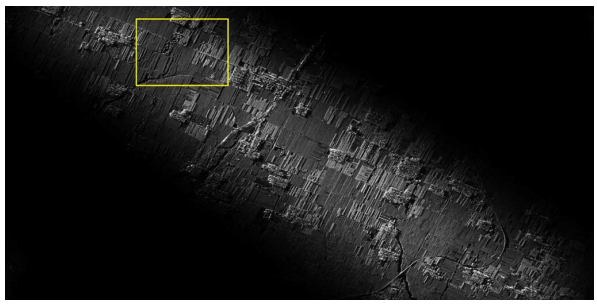

Fig. 19. Image with INS and SPGA.

APPENDIX A

In (31), we extend $\vartheta(\Delta K_y, K_x^*)$ into Taylor series at $\Delta K_y = 0$. And we have

$$\vartheta(\Delta K_y, K_x^*)|_{\Delta K_y=0} = -K_{rc} \cdot \Delta R_{err}(X). \tag{A1}$$

And the first order coefficient is given by

$$\left.\frac{\partial \vartheta(\Delta K_y, K_x^*)}{\partial \Delta K_y}\right|_{\Delta K_y=0} = -\left\{\frac{\partial K_r}{\partial \Delta K_y}\Delta R_{err}(X^*)\right\}\Big|_{\substack{\Delta K_y=0 \\ X^*=X}} - \left\{K_r \frac{\partial \Delta R_{err}(X^*)}{\partial X^*}\frac{\partial X^*}{\partial K_r}\frac{\partial K_r}{\partial \Delta K_y}\right\}\Big|_{\substack{\Delta K_y=0 \\ X^*=X}} \tag{A2}$$

where

$$\left.\frac{\partial K_r}{\partial \Delta K_y}\right|_{\Delta K_y=0} = \left.\frac{\sqrt{K_{rc}^2 - K_x^2}}{\cos\varphi\sqrt{\left(\frac{\Delta K_y}{\cos\varphi} + \sqrt{K_{rc}^2 - K_x^2}\right)^2 + K_x^2}}\right|_{\Delta K_y=0} = \frac{\sqrt{K_{rc}^2 - K_x^2}}{\cos\varphi K_{rc}} \tag{A3a}$$

$$\left.\frac{\partial K_r}{\partial \Delta K_y}\right|_{\Delta K_y=0} = \left.\frac{\sqrt{K_{rc}^2 - K_x^2}}{\cos\varphi K_{rc}}\right|_{\Delta K_y=0} = \left.\frac{r}{\sqrt{(\cos\varphi\cdot r)^2 + (X - r\sin\varphi - x)^2}}\right|_{\Delta K_y=0} \approx 1 \tag{A3b}$$

$$\left.\frac{\partial X^*}{\partial K_r}\right|_{\substack{\Delta K_y=0 \\ K_x=K_x^*}} = \left.\frac{K_x K_r}{\sqrt[3]{K_r^2 - K_x^2}} r\cos\varphi\right|_{\substack{\Delta K_y=0 \\ K_x=K_x^*}} = -\frac{(X - r\sin\varphi - x)\sqrt{(\cos\varphi\cdot r)^2 + (X - r\sin\varphi - x)^2}}{K_{rc}\cos^2\varphi\cdot r} \approx \frac{r\sin\varphi}{K_{rc}\cos^2\varphi} \tag{A3c}$$

$$\left.\frac{\partial \Delta R_{err}(X^*)}{\partial X^*}\right|_{\substack{\Delta K_y=0 \\ K_x=K_x^*}} = 2e_2X + 3e_3X^2 + 4e_4X^3\cdots \tag{A3d}$$

$$\left.\frac{\partial \varphi(\Delta K_y, K_x^*)}{\partial \Delta K_y}\right|_{\Delta K_y=0} = -\Delta R_{err}(X) - \frac{r\sin\varphi}{\cos^2\varphi}\cdot\left(2e_2X + 3e_3X^2 + 4e_4X^3\cdots\right). \tag{A3e}$$

Hence, we have

$$\Delta R'_{err}(X) = \Delta R_{err}(X) + \frac{r\sin\varphi}{\cos^2\varphi}\cdot\left(2e_2X + 3e_3X^2 + 4e_4X^3\cdots\right). \tag{A4}$$

And the analytic expression of $\varphi(\Delta K_y, K_x^*)$ is approximated as

$$\vartheta(\Delta K_y, K_x^*) \approx -K_{rc}\cdot\Delta R_{err}(X) - \Delta K_y \cdot\left[\Delta R_{err}(X) + \frac{r\sin\varphi}{\cos^2\varphi}\cdot\left(2e_2X + 3e_3X^2 + 4e_4X^3\cdots\right)\right]. \tag{A5}$$

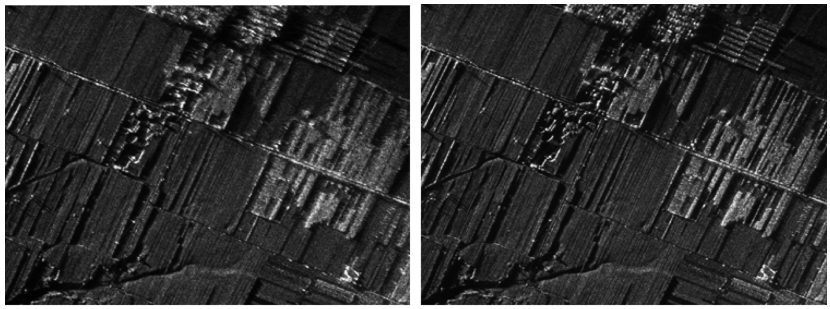

(a) (b)

Fig. 20. Image comparison. (a) Magnified local image from Fig. 13. (b) Magnified local image from Fig. 19.

APPENDIX B

Extending $E(X;r,x)$ into Taylor series with respect to X round origin, we have approximates that

$$E(X;r,x) \approx E(0;r,x) + E'(0;r,x)X + \frac{1}{2}E''(0;r,x)X^2 \tag{B1}$$

where the Taylor coefficients are given by

$$E(0;r,x) = \sin\varphi \tag{B2a}$$

$$E'(0;r,x) = -\frac{\cos^2\varphi}{r} \tag{B2b}$$

$$E''(0;r,x) = \frac{3\left(\sin\varphi + \sin^3\varphi\right)}{r^2}. \tag{B2c}$$

Similarly, we also have

$$F(X;r,x) \approx F(0;r,x) + F'(0;r,x)\cdot X \tag{B3}$$

where the corresponding coefficients are

$$F(0;r,x) = \frac{\cos^2\varphi}{2r} \tag{B4a}$$

$$F'(0;r,x) = \frac{3\sin\varphi\cos^2\varphi}{2r^2}. \tag{B4b}$$

Then, the analytic expression of signal after deramping is approximated by

$$\begin{aligned} &s'_{sm}(y,X) \\ &\approx \exp\left\{-jK_{rc}\left[\alpha_0(r,x) + \alpha_1(r,x)\cdot X + \alpha_2(r,x)\cdot X^2\right]\right\} \\ &\quad\times \exp\left[-jK_{rc}\cdot\Delta R_{err}(X)\right] \end{aligned} \tag{B5}$$

where

$$\alpha_0(r,x) = -\sin\varphi\cdot x + \frac{\cos^2\varphi}{2r}\cdot x^2 \tag{B6a}$$

$$\alpha_1(r,x) = E'(0;r,x)\,x + F'(0;r,x)\,x^2 \tag{B6b}$$

$$\alpha_2(r,x) = \frac{1}{2}E''(0;r,x)\,x. \tag{B6c}$$

ACKNOWLEDGMENT

The authors thank the anonymous reviewers for their valuable comments to improve the paper quality.

REFERENCES

[1] W. G. Carrara, R. S. Goodman, and R. M. Majewski, *Spotlight Synthetic Aperture Radar: Signal Processing Algorithm [M]*. Boston, MA: Artech House, 1995.

[2] R. K. Raney, H. Runge, R. Bamler, I. G. Cumming, and F. H. Wong, "Precision SAR processing using chirp scaling," *IEEE Trans. Geosci. Remote Sens.*, vol. 32, pp. 786–799, Jul. 1994.

[3] A. Moreira and H. Yonghong, "Airborne SAR processing of highly squinted data using a chirp scaling approach with integrated motion compensation," *IEEE Trans. Geosci. Remote Sens.*, vol. 32, no. 5, pp. 1029–1040, Sep. 1994.

[4] G. W. Davidson, I. G. Cumming, and M. R. Ito, "A chirp scaling approach for processing squint mode SAR data," *IEEE Trans. Aerosp. Electron. Syst.*, vol. 32, no. 1, pp. 121–133, Jan. 1996.

[5] C. Cafforio, C. Prati, and F. Rocca, "SAR data focusing using seismic migration techniques," *IEEE Trans. Aerosp. Electron. Syst.*, vol. 27, no. 2, pp. 194–207, 1991.

[6] R. Bamler, "A comparison of range-Doppler and wavenumber domain SAR focusing algorithms," *IEEE Trans. Geosci. Remote Sens.*, vol. 30, no. 4, pp. 706–713, Sep. 1992.

[7] G. Cumming, Y. L. Neo, and F. Hong, "Interpretations of the Omega-k algorithm and comparisons with other algorithms," in *Proc. IGARSS*, Toulouse, France, 2003, pp. 1455–1458.

[8] A. Reigber, E. Alivizatos, A. Potsis, and A. Moreira, "Extended wavenumber-domain synthetic aperture radar focusing with integrated motion compensation," *IEE Proc.—Radar Sonar Navig.*, vol. 153, no. 3, pp. 301–310, Jun. 2006.

[9] E. Alivizatos, A. Reigber, and A. Moreira, "SAR processing with motion compensation using the extended wavenumber algorithm," in *Proc. EUSAR*, Ulm, Germany, 2004, pp. 157–160.

[10] M. Vandewal *et al.*, "Efficient and precise processing for squinted spotlight SAR through a modified Stolt mapping," *EURASIP J. Adv. Signal Process.*, vol. 2007, pp. 1–10.

[11] A. W. Doerry, "Automatic compensation of antenna beam roll-off in SAR images," Sandia, 2006, Rep. SAND2006-2632.

[12] J. C. Kirk, "Motion compensation for synthetic aperture radar," *IEEE Trans. Aerosp. Electron. Syst.*, vol. AES-11, no. 3, pp. 338–348, May 1975.

[13] G. W. Davidson and I. Cumming, "Signal properties of spaceborne squint-mode SAR," *IEEE Trans. Geosci. Remote Sens.*, vol. 35, no. 3, pp. 611–617, May 1997.

[14] S. N. Madsen, "Estimating the Doppler centriod of SAR data," *IEEE Trans Aerosp. Electron. Syst.*, vol. 25, no. 2, pp. 134–140, Mar. 1989.

[15] F. H. Wang and I. G. Cumming, "A combined SAR Doppler centroid estimation scheme based upon signal phase," *IEEE Trans. Geosci. Remote Sens.*, vol. 34, no. 3, pp. 696–707, May 1996.

[16] M. Xing, X. Jiang, R. Wu, F. Zhou, and Z. Bao, "Motion compensation for UAV SAR based on raw radar data," *IEEE Trans. Geosci. Remote Sens.*, vol. 47, no. 8, pp. 2870–2883, Aug. 2009.

[17] J. T. G. Partida, P. A. Gonzalez, and M. B. Garcia, "SAR System for UAV operation with motion error compensation beyond the resolution cell," *Sensors*, vol. 8, pp. 3384–3405, 2008.

[18] G. Fornaro, E. Sansosti, R. Lanari, and M. Tesauro, "Role of processing geometry in SAR raw data processing," *IEEE Trans. Aerosp. Electron. Syst.*, vol. 38, no. 2, pp. 441–454, Apr. 2002.

[19] I. G. Cumming and F. H. Wong, *Digital Processing of Synthetic Aperture Radar Data: Algorithms and Implementation*. Norwood, MA: Artech House, 2005.
[20] Meta, P. Hoogeboom, and L. P. Ligthart, "Signal processing for FMCW SAR," *IEEE Trans. Geosci. Remote Sens.*, vol. 45, no. 11, pp. 3519–3532, Nov. 2007.
[21] Z. Jiang, K. Huang-Fu, and J. Wan, "A chirp transform algorithm for processing squint mode FMCW SAR data," *IEEE Geosci. Remote Sens. Lett.*, vol. 4, no. 3, pp. 377–381, Jul. 2007.
[22] R. Wang, O. Loffeld, H. Nies, S. Knedlik, M. Hägelen, and H. Essen, "Focus FMCW SAR data using the wavenumber domain algorithm," *IEEE Trans. Geosci. Remote Sens.*, vol. 48, no. 4, pp. 2109–2118, Apr. 2007.
[23] D. E. Wahl, P. H. Eichel, D. C. Ghiglia, and C. V. Jakowatz Jr., "Phase gradient autofocus—A robust tool for high resolution phase correction," *IEEE Trans. Aerosp. Electron. Syst.*, vol. 30, no. 3, pp. 827–835, Jul. 1994.
[24] K. A. C. de Macedo, R. Scheiber, and A. Moreira, "An autofocus approach for residual motion errors with application to airborne repeated-pass SAR interferometry," *IEEE Trans. Geosci. Remote Sens.*, vol. 46, no. 10, pp. 3151–3162, Oct. 2008.
[25] H. L. Chan and T. S. Yeo, "Noniterative quality phase-gradient autofocus (QPGA) algrotihm for spotlight SAR imagery," *IEEE Trans. Geosci. Remote Sens.*, vol. 36, no. 5, pp. 1531–1539, Sep. 1998.
[26] W. Ye, T. S. Yeo, and Z. Bao, "Weighted least-squares estimation of phase errors for SAR/ISAR autofocus," *IEEE Trans. Geosci. Remote Sens.*, vol. 37, no. 5, pp. 2487–2494, Sep. 1999.
[27] A. W. Doerry, "Autofocus correction of excessive migration in synthetic aperture radar images," Sandia, 2004, Rep. SAND2004-4770.
[28] D. E. Wahl, C. V. Jakowatz Jr., P. A. Thompson, and D. C. Ghiglia, "New approach to strip-map SAR autofocus," in *Proc. 6th IEEE Digital Signal Process. Workshop*, Oct. 1994, pp. 53–56.
[29] D. G. Thompson, J. S. Bates, D. V. Arnold, and D. G. Long, "Extending the phase gradient autofocus algorithm for low-altitude stripmap mode SAR," in *Proc IGARSS*, Jul. 1999, pp. 564–566.

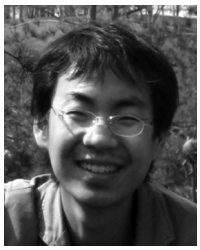

Lei Zhang was born in Zhejiang Province, China in 1984. He received the B.S. degree in mechanism and electrical engineering from Chang'an University, Xi'an, China, in 2006, and is currently working toward Ph.D. degree in signal and information processing at the National Key Lab of Radar Signal Processing, Xidian University, Xi'an, China.

His major research interests are radar imaging (SAR/ ISAR).

Jialian Sheng was born in Zhejiang Province, China, 1987. She received the B.S. degree in biomedical engineering from Xidian University, Xi'an, China, in 2010, and is currently working toward the Ph.D. degree in signal and information processing from the National Lab for Radar Signal Processing at the same university.

Her major research interests are radar signal processing and sparse optimization.

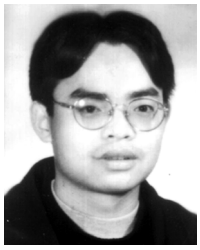

Mengdao Xing (M'04) was born in Zhejiang, China, in November, 1975. He received the B.Eng. and Ph.D. degrees in electrical engineering from Xidian University, Xi'an, China in 1997 and 2002, respectively.

He is currently a Full Professor with the National Key Laboratory for Radar Signal Processing, Xidian University. His research interests include SAR, ISAR, and over the horizon radar (OTHR).

Zhijun Qiao (M'10) received the Ph.D. degree in applied math from the Institute of Mathematics, Fudan University, Shanghai, China, in 1997.

From 1999 to 2001, he was a Humboldt Research Fellow with the Department of Mathematics and Computer Science, University of Kassel, Kassel, Germany. From 2001 to 2004, he was a Researcher with the Theoretical Division, Los Alamos National Laboratory, Kassel, Germany. He has also been a Professor with the Department of Mathematics, Liaoning University, Shenyang City, China, since 1997 and is currently with the Department of Mathematics, The University of Texas-Pan American, Edinburg, U.K. He is currently the Editor-in-Chief of the *Pacific Journal of Applied Mathematics*. He has published two monographs and more than 90 articles in peer-reviewed international journals. His research interest includes nonlinear partial differential equations and its application in radar imaging.

Dr. Qiao's dissertation was one of the first 100 excellent Ph.D. dissertations awarded in 1999. He is the PI of two grants under the Department of Defense Program and the Norman Hackerman Advanced Research Program.

Tao Xiong was born in Hubei Province, China in 1984. He received the B.S. degree in measuring and control technology and instrumentations from Xidian University, Xi'an, China, in 2006, where he is currently working toward the Ph.D. degree in signal processing and information from the National Key Lab of Radar Signal Processing.

His major research interests are radar imaging (Bistatic SAR/ISAR).

Zheng Bao (M'80–SM'90) was born in Jiangsu, China. He received the B.S. degree from the Communication Engineering Institute of China in 1953.

Currently, he is a Professor with Xidian University, Xi'an, China, and the chairman of the academic board of the National Key Lab of Radar Signal Processing, Xidian University. He has authored or coauthored six books and published over 300 papers. Now, his research fields include space-time adaptive processing (STAP), radar imaging (SAR/ISAR), automatic target recognition (ATR) and over-the-horizon radar (OTHR) signal processing.

Professor Bao is a member of the Chinese Academy of Sciences.